

Andrews University

Digital Commons @ Andrews University

Faculty Publications

4-14-2023

Information Horizon of Solar Active Regions

Jay R. Johnson

Andrews University, jrj@andrews.edu

Simon Wing

Johns Hopkins University, simon.wing@jhupl.edu

Carson O'ffill

Andrews University, offill@andrews.edu

Bishwa Neupane

Andrews University

Follow this and additional works at: <https://digitalcommons.andrews.edu/pubs>



Part of the [Astrophysics and Astronomy Commons](#), and the [Engineering Commons](#)

Recommended Citation




Johnson, Jay R.; Wing, Simon; O'ffill, Carson; and Neupane, Bishwa, "Information Horizon of Solar Active Regions" (2023). *Faculty Publications*. 4650.

<https://digitalcommons.andrews.edu/pubs/4650>

This Article is brought to you for free and open access by Digital Commons @ Andrews University. It has been accepted for inclusion in Faculty Publications by an authorized administrator of Digital Commons @ Andrews University. For more information, please contact repository@andrews.edu.



Information Horizon of Solar Active Regions

Jay R. Johnson¹ , Simon Wing² , Carson O'ffill¹, and Bishwa Neupane¹ ¹ Andrews University Berrien Springs, Michigan, USA² Johns Hopkins University Laurel, Maryland, USA; simon.wing@jhuapl.edu

Received 2022 December 12; revised 2023 March 16; accepted 2023 March 20; published 2023 April 14

Abstract

Information theory is used to characterize the solar active region periodicities and memories from the Carrington map images 1974–2021. The active regions typically evolve and move from one map to the next. In order to track these active region structures in sequences of images, an innovative method based on information theory is developed. Image entropy provides a measure of the organization of structures in the images. The entropy can also be used as a filter to identify structures and partition the active regions, which are then registered for each image. The partitions are used to compute the mutual information and measure the information flow from the active regions from one image to the next. Finally, conditional mutual information is used to give a measure of the information flow from one image to another given the third image. The results suggest the following: (1) there is a long-term memory of two cycles or more; (2) the coherence time of the active regions is ~ 2 yr; and (3) the average active region structure scale size carrying the most information is approximately 118×10^3 – 236×10^3 Mm². The study has implications to the short- and long-term predictability of active regions and sunspots as well as the nature of flux transport at the Sun. Finally, our innovative method can be similarly applied to stellar data to determine the dynamics of the active regions of stars.

Unified Astronomy Thesaurus concepts: [Solar active regions \(1974\)](#); [Solar cycle \(1487\)](#); [Sunspots \(1653\)](#); [Solar dynamo \(2001\)](#); [Solar magnetic bright points \(1984\)](#); [Magnetogram \(2359\)](#)

1. Introduction

Solar activity is often inferred from the number of magnetically active regions, which often appear as dark regions or sunspots on the photosphere of the Sun. The number of sunspots increases and decreases with a periodicity of about 11 yr often referred to as the solar cycle. Predicting the sunspot number (SSN), which has space weather implications, has been difficult and challenging due to the complexity of the solar dynamo (Pesnell 2016).

In the Babcock–Leighton model (Babcock 1961; Leighton 1964, 1969), the solar cycle is a manifestation of the cyclical conversion of the poloidal to toroidal magnetic fields (see review in Charbonneau 2020). The meridional flow, which acts like a conveyor belt, carries the poloidal field to the polar region and then down to the bottom of the convection zone or tachocline and then to lower latitude. As the flux is transported to lower latitude, the differential rotation shears the magnetic field leading to the growth of the toroidal field. The shearing motion creates regions of strong magnetic field, which are buoyant and subsequently rise to the surface (photosphere). The Coriolis force acting on the rising toroidal field causes the emerging fluxes to appear as pairs of sunspot with a slight tilt such that the following spot of the pair tends to be further from the equator than the preceding spot (Joy's law), leading to the growth of the poloidal field. The meridional flow subsequently transports the poloidal field, which has the opposite polarity than that of the old polar field, to higher latitude. This process continues until a new poloidal field with the opposite polarity is established, which commences a new solar cycle. Over the next cycle, the poloidal field reverts back to the original polarity giving rise to an overall 22 yr periodicity.

In many flux transport models, the meridional flow in the convection zone can be characterized by advection with low diffusivity, particularly at the bottom of the convection zone or tachocline, implying the possibility for a long-term memory of previous cycles and solar cycle predictability (Dikpati & Charbonneau 1999). In the model of Charbonneau & Dikpati (2000), the slow transport speed at the bottom of convection zone or tachocline results in memory of the previous two cycles. Similarly, in the models of Dikpati et al. (2004) and Dikpati & Gilman (2006), the convection is highly dominated by advection, and their models exhibit long-term memory—three cycles or even longer. Charbonneau & Barlet (2011) found that the polar field is well correlated with the amplitude of the next cycle only when there is a connection between the surface and interior layers. However, advection-dominated transport driven by a randomly fluctuating meridional flow may reduce cycle memory.

In contrast, in flux transport models where diffusion dominates the transport, the memory is found to be short—about one cycle (Choudhuri et al. 2007; Jiang et al. 2007; Muñoz-Jaramillo et al. 2013a; Muñoz Jaramillo et al. 2013b; Cameron & Schüssler 2016). Yeates et al. (2008) hypothesized that stronger diffusion destroys the polar field faster and short-circuits the meridional circulation, shortening the memory of the previous cycles. Other factors that can affect the memory include hemispherical asymmetry where the conveyor belt can cross the equator, changing its profile, and transport by turbulent pumping (Guerrero & de Gouveia Dal Pino 2008).

The solar magnetic cycle is challenging to model and predict because the solar dynamo is a nonlinear and complex system (Tobias 1997; Beer et al. 1998; Knobloch et al. 1998; Wilmot-Smith et al. 2005), where the standard linear correlational analysis may be inadequate. On the other hand, information theory can determine linear and nonlinear correlations and the amount of information transfer between variables. Information theory has been used successfully in the studies of the Earth's



Original content from this work may be used under the terms of the [Creative Commons Attribution 4.0 licence](#). Any further distribution of this work must maintain attribution to the author(s) and the title of the work, journal citation and DOI.

magnetosphere and ionosphere (Johnson & Wing 2005; Balasis et al. 2013; Johnson & Wing 2014; Wing et al. 2016; De Michelis et al. 2017; Johnson et al. 2018; Osmane et al. 2022; Wing et al. 2022). It has been used to give a measure linear and nonlinear correlation between energetic neutral atoms and 5 kHz narrowband radio wave emissions at Saturnian magnetosphere (Wing et al. 2020).

In the studies of the Sun, information theory has been used to establish the amount of information transfer and its timescales among polar field (proxy for poloidal field), sunspots (proxy for toroidal field), and meridional flow (Wing et al. 2018; Wing & Johnson 2019). More recently, it has been used to determine the short-term memory of solar flares (Snelling et al. 2020; Rivera et al. 2022a, 2022b).

In the present study, the Carrington map image is used to provide a measure of the Sun’s magnetic field strength and active regions. We use an innovative information theoretic tool to investigate the flow of information from active regions in one map to the next over several solar cycles. We examine how much information the past active regions provide about their future. We also examine the spatial scale of the active regions as well as the decay timescale of the structures in these regions. The present study can shed a new light on the predictability of the active regions and sunspots from an observational perspective.

2. Data Set

The sunspot number record is obtained from Sunspot Index and long-term Solar Observations (SILSO) website, <https://www.sidc.be/silso/home>. The Carrington map images are obtained from <http://wso.stanford.edu/synopticl.html>. We use a sequence of 597 consecutive Carrington map images from 1974 to 2021 covering solar cycles 21–24. These maps provide magnetic field measurements up to $\pm 75^\circ$ latitude with a resolution of approximately 5° .

3. Methods

3.1. Image Entropy and Hilbert–Huang Transform

The number of active regions and sunspots (proxies for the toroidal field) varies with solar cycle. Accordingly, the Carrington map images have more variations, structures, and complexities near solar maximum than solar minimum. We use image entropy as a way to quantify the image complexity. Image entropy gives a measure of the disorder in the image.

We normalize the value of each pixel in the image with respect to the maximum and minimum value of the entire data set of 597 maps. For each image, we bin the pixel luminosity (pixel value) into 256 bins and then calculate the image entropy, which is given by

$$H = -\sum P_i \log_2(P_i). \quad (1)$$

P_i is the probability of each pixel value.

Figure 1(a) shows the image entropy for each Carrington rotation from 1974 to 2021 (blue curve). Generally, the image entropy increases with the number of active regions or sunspots, as expected. More active regions lead to more structures and more complexities in the image. For comparison with the sunspots, Figure 1(a) also plots the sunspot number (red curve). The figure shows that image entropy tracks the

sunspot number very well. The deep minima seen in solar cycle 24 (around 2008) and 25 (around 2019) in the sunspot number (red curve) are also seen in the corresponding image entropy (blue curve). Moreover, the continuing downward trend in the sunspot number is also evident in image entropy.

Similar to sunspots, the image entropy also exhibits a periodicity. Figure 1(b) displays the autocorrelation of the image entropy shown in Figure 1(a). This figure shows that the image entropy has a periodicity of about 140 Carrington cycles, which is about 1 solar cycle timescale. It is to be noted that subsequent peaks are not located at lags of 280 and 420 indicating that activity cycle is not purely sinusoidal and likely has several modes of oscillation. It is well known the solar cycle duration is not always fixed exactly at 11 yr, but rather it can vary from one cycle to the next. It is also interesting to note that the autocorrelation appears to increase three cycles ahead.

To examine this feature further, we apply a Hilbert–Huang transform (Huang & Wu 2008; Barnhart & Eichinger 2011), to the monthly sunspot number for this same time period, which can give a measure of the instantaneous frequency of a time-variable system. The transform starts by using empirical mode decomposition to obtain the intrinsic mode functions. These mode functions are the basis of the Hilbert spectral analysis, which is shown in Figure 1(c).

The Hilbert spectrum provides the instantaneous frequency of the intrinsic mode functions. The strongest mode has a period of approximately 140 Carrington cycles or about 1 solar cycle with some variability, which can be seen at $f/f_s = 1$ ($f_s = 140$ Carrington rotations) in Figure 1(c). Note, however, the presence of a weaker mode at about $f/f_s = 0.5$, which is about 280 Carrington cycles or about 23 yr. This longer cycle provides evidence of a two solar cycle effect and an asymmetry between polarity of the cycles, which was first identified by Gnevyshev & Ohl (1948). Additional variability having longer timescales of 60–120 yr (Gleissberg cycle) have also been identified in the historical monthly sunspot number sequence dating back to the 1749 (Barnhart & Eichinger 2011). The existence of overlap between cycles and asymmetries has also recently been pointed out by (McIntosh et al. 2015; McIntosh & Leamon 2017, and references therein) and may be reflected in this $f/f_s = 0.5$ mode. Besides these two main modes, Figure 1(c) shows that there are also weaker higher frequency modes, $f/f_s > 1$, corresponding to periodicities of < 1 solar cycle. Unlike the two main modes, these higher frequency modes sporadically appear and disappear within a cycle in the solar cycles 21–24. Previous studies reported that some high frequencies, e.g., Rieger-type periodicities (periodicities of several Carrington rotations) and intermediate-term periodicities (periodicities of 4–20 Carrington rotations), appear and disappear within one cycle (Lean & Brueckner 1989; Zaqarashvili 2010, and references therein). Interestingly, there is a frequency mode at $f/f_s = 2.5\text{--}3$ or a periodicity around 45–50 Carrington rotations (3.5–4 yr) near the minimum of solar cycle 24 (yr 2010–2012). We will explore these periodicities further in Section 5.

3.2. Mutual Information

While the correlation provides some indication of how active regions evolve, it is even more instructive to examine the information flow between a sequence of maps. To do this, we use mutual information (MI) and conditional mutual

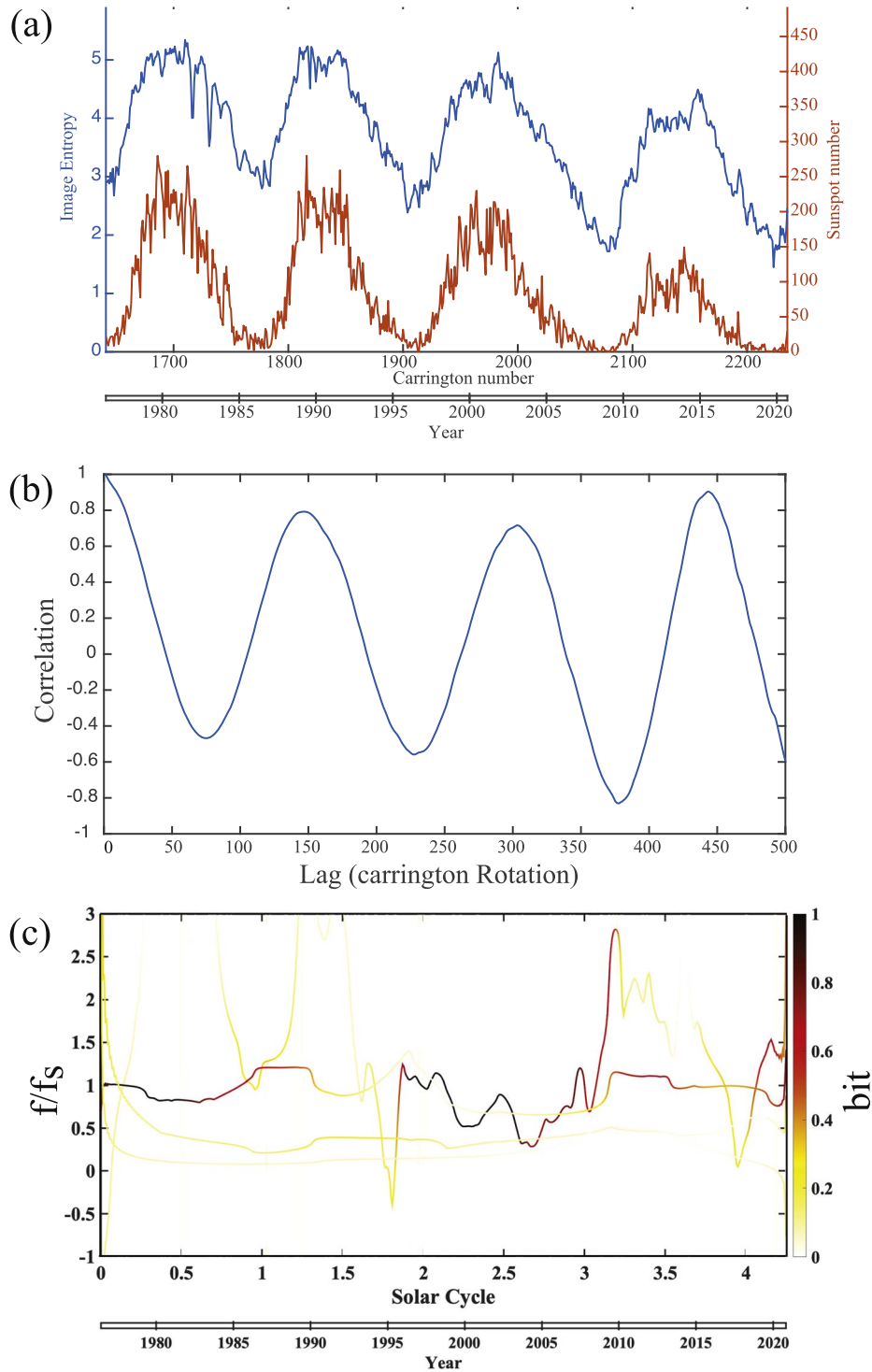


Figure 1. (a) The image entropy of normalized Carrington map image (blue) and the sunspot number (red) as a function of Carrington number and Gregorian year. (b) The autocorrelation of the image entropy as a function of the lag time in Carrington rotation. The autocorrelation peaks at about 1, 2, and 3 solar cycle timescale. (c) Hilbert–Huang transform showing the frequencies of the dominant intrinsic mode functions as a function of Gregorian year and time since 1974. Note the strong mode at the frequency of the solar cycle, $f/f_s = 1$ ($f_s = 140$ Carrington rotations) and a weaker mode at half the frequency, $f/f_s = 0.5$ (or 2 solar cycles).

information (CMI), which are briefly summarized below, but they are also described in (Balasis et al. 2013), and Wing et al. (2016, 2018, 2022). MI compares the uncertainty of measuring variables jointly with the uncertainty of measuring the two variables independently. $MI(X, Y)$ gives a measure of linear and nonlinear dependence between X and Y . $CMI(X, Y|Z)$ gives a measure of MI between X and Y given Z .

For two integer time series X and Y , the mutual information (in units of bits) is defined by

$$I(X, Y) = H(X) + H(Y) - H(X, Y) \quad (2)$$

where,

$$H(X) = -\sum_{x \in X} P_X(x) \log_2(P_X(x)) \quad (3)$$

$$H(X) = - \sum_{y \in Y} P_Y(y) \log_2(P_Y(y)) \quad (4)$$

$$H(X, Y) = - \sum_{x \in X; y \in Y} P_{XY}(x, y) \log_2(P_{XY}(x, y)). \quad (5)$$

H is entropy, $P_X(x)$ is the measured probability of the random variable X taking in the value x , and $P_{XY}(x, y)$ is the joint probability of observing random variable X having the value x and Y having the value y .

The conditional mutual information gives the expected value of the mutual information of two random variables X and Y given the value of a third Z .

$$\text{CMI}(X; Y|Z) = H(X, Z) + H(Y, Z) - H(X, Y, Z) - H(Z) \quad (6)$$

One substantial challenge to measuring information flow from one map to the next is the motion of structures in latitude and longitude. Two images may have similar features; however, if these features move between images, the mutual information drops drastically. This issue leads to a misleading loss of mutual information between structures. To solve this issue, the prominent features need to be aligned before calculating the mutual information. The alignment can be done by identifying the features in the image, isolating them, then registering each isolated region to its most likely counterpart.

To accomplish this task, an entropy filter is used. A 3×3 neighborhood of pixels is chosen to calculate the local image entropy, which highlights the features corresponding to active solar regions. An example is presented in Figure 2. Figure 2(a) shows the original image while Figure 2(b) shows the result of applying entropy filter to the image in Figure 2(a). The figure shows that active regions generally have higher entropies than the rest of the image due to a higher variation in the magnetic field.

To isolate the regions of high entropy (e.g., active regions), a threshold is applied to the filtered image in Figure 2(b). Pixel values less than 2.05 are set to 0 in this case while all other values are set to 1. This creates a mask, which is shown in Figure 2(c). The mask can then be multiplied by the original image (Carrington map) in Figure 2(a), resulting in Figure 2(d). This operation effectively isolates and selects the high-entropy regions.

Finally, each separate partition is cropped from the image, forming a set of partitions, which are highlighted by the red boxes in Figure 2(d). This process is performed on all images (Carrington maps), transforming the data set from images to sets of partitions containing prominent features.

4. Image Mutual Information

Once the partitions of each image are registered, we compute the mutual information between two images (A and B) based on the set of partitions ($A_1, A_2, \dots, A_n \in A$ and ($B_1, B_2, \dots, B_m \in B$). Without loss of generality, we assume that the number of partitions of A is less than or equal to the number of partitions in B , i.e., $n \leq m$. We next compute the mutual information between all partitions, $\text{MI}(A_i, B_j)$. Once this step is completed, we identify the pair of partitions having the largest mutual information, and we relabel the elements of A and B so that $\text{MI}(A_1, B_1)$ is largest value of the mutual information. We then consider the remaining pairs of partitions ($A_{i>1}, B_{j>1}$) and

relabel the remaining elements of A and B such that $\text{MI}(A_2, B_2)$ has the largest remaining mutual information. This procedure is continued until all partitions A have been paired with a partition of B . The mutual information of the two images is then computed as $\text{MI}(A, B) = \sum_{i=1}^n \text{MI}(A_i, B_i)$.

When considering the mutual information between images separated by τ Carrington rotations, we consider the ensemble average over all pairs of images having a separation τ . Figure 3 shows the result of calculating the mutual information of image (t) and image(t+ τ) for $\tau = 1-500$ Carrington rotations. The mutual information drops off gradually at a timescale of about 20 Carrington rotation, suggesting a timescale over which the active region structures remain coherent.

To determine the significance of the mutual information over these time lags, we scramble the pixels in the partitions of one of the images and determine the resulting mutual information. The scrambling procedure is performed multiple times and averaged. The mutual information of the active regions is then compared with the mean of the surrogate (scrambled) active regions and compared relative to the standard deviation (σ) of the surrogates. In Figure 3, all $\text{MI} > 3\sigma$ and hence they are all significant.

5. Short- and Long-term Memory of the Active Regions

In the autocorrelation of the image entropy plotted in Figure 1(b), the autocorrelation appears to increase three cycles ahead suggesting complicated oscillation modes. Similar pattern can be seen in the mutual information plotted in Figure 3. Moreover, the Hilbert–Huang transform shown in Figure 1(c) suggests the presence of multiple modes with periodicities < 1 solar cycle, ~ 11 yr (1 solar cycle), ~ 23 yr (2 solar cycles), or even longer.

Furthering our analysis, we determine whether there is a relationship between active regions that persists for two or more cycles given that we know the properties of the active region in the last cycle. In order to do this, we consider image conditional mutual information (CMI) of the sequence of maps. The conditional mutual information makes it possible to determine the similarity of two images given a third image. The main objective is to see whether there is evidence of memory in the solar cycle beyond the most recent cycle. To examine this question, we compute $\text{CMI}(c(t+\tau), c(t-\Delta)|c(t))$, which calculates the mutual information between Carrington map(c) at $t+\tau$ and $t-\Delta$ given the Carrington map at time t . Figure 4 shows the results of the CMI. In the figure, all $\text{CMI} > 3\sigma$ and hence are all significant.

Several features in this plot are worth noting. The most obvious features are the diagonal lines of enhanced CMI. These lines occur when $\tau + \Delta$ is a multiple of 140, suggesting that there is a general similarity between the map separated by a solar cycle, which perhaps can be expected. However, along the diagonal lines there is substantial variation with obvious peaks at $\tau \approx 1-20, 140-160, \dots$. However, the recurrence of the peaks after a solar cycle suggests a long-term memory lasting two or possibly more solar cycles. The peak at τ and $\Delta \sim 140$ (where the dashed gray lines intersect) shows that there is additional information from the Carrington map two solar cycles ago in addition to what is known one solar cycle ago. Thus, it suggests a memory of two solar cycles. There is a smaller peak at $\tau \sim 330$ and $\Delta \sim 140$, suggesting a longer memory. The long-term memory obviously decreases with time

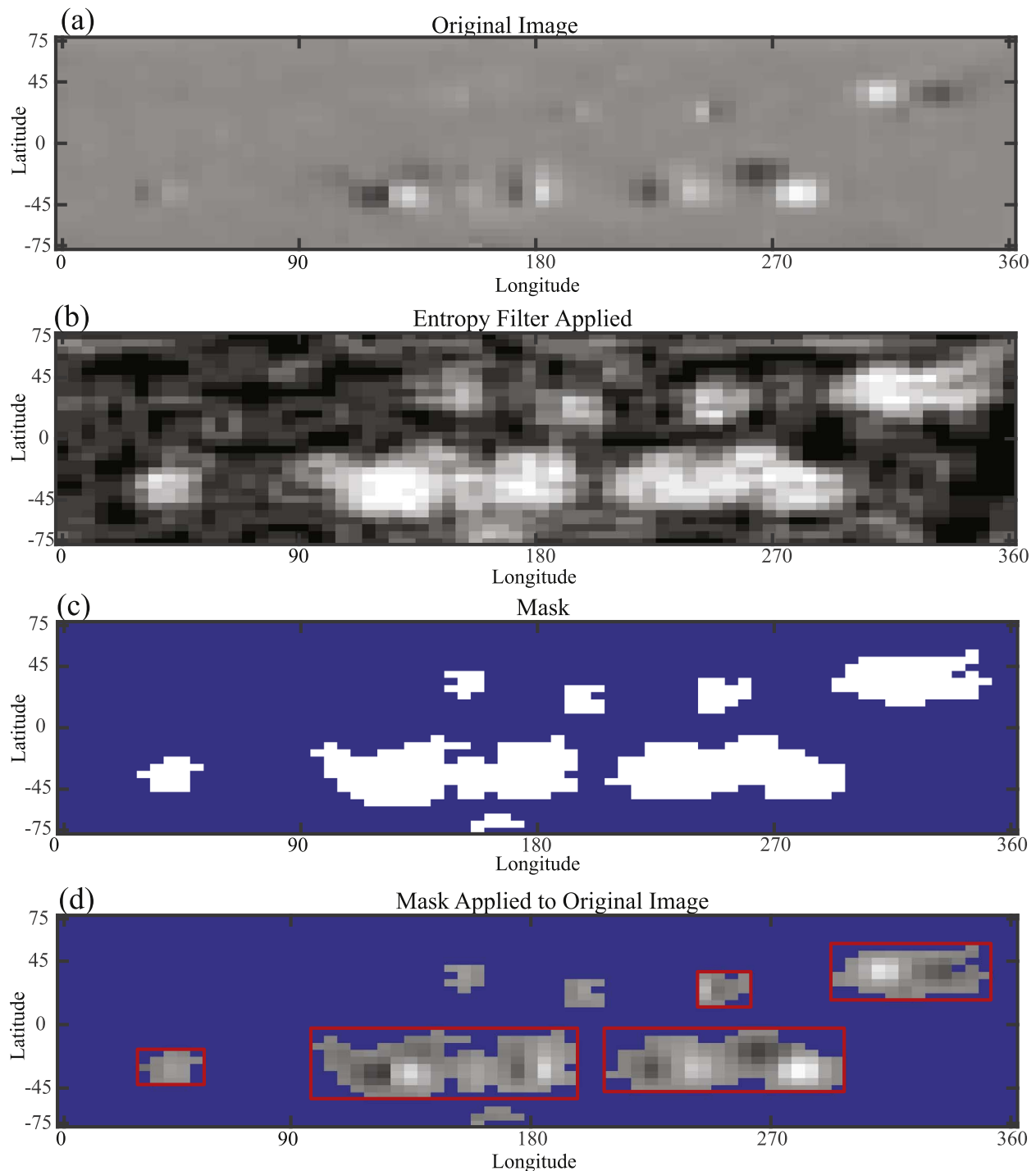


Figure 2. An entropy filter is applied to original Carrington map image (a) to identify active region structures, which show up as regions with high entropies (b). Image (d) is obtained by multiplying the image mask (c), constructed from thresholding image (b), with the original image (a). This procedure effectively identifies and partitions the active regions in image (a). The partitions are bounded by the red rectangles in image (d).

as expected. The results here highlight the dynamics of the active regions and have implications for the predictability of the active region structures and sunspots. A long-term memory of two solar cycle or more has also been found in Wing et al. (2018), which examined information transfer from past polar fields to the sunspot number at the Sun. The study found that the polar field of the last two solar cycles or even further back carries some information about the sunspot number.

The width of these peaks, about 20 Carrington cycles, may suggest the coherence time (short term memory) of solar active

regions is ~ 2 yr. This timescale may be consistent with previous studies that found that the lifetimes of large active regions (superactive regions, active zones) can range from months to several years (Bai 1987). The spatial scale of our active regions is discussed in the next section.

6. Spatial Scale of Active Regions

While this study investigates the temporal coherence of the structures, we are also able to investigate the spatial coherence

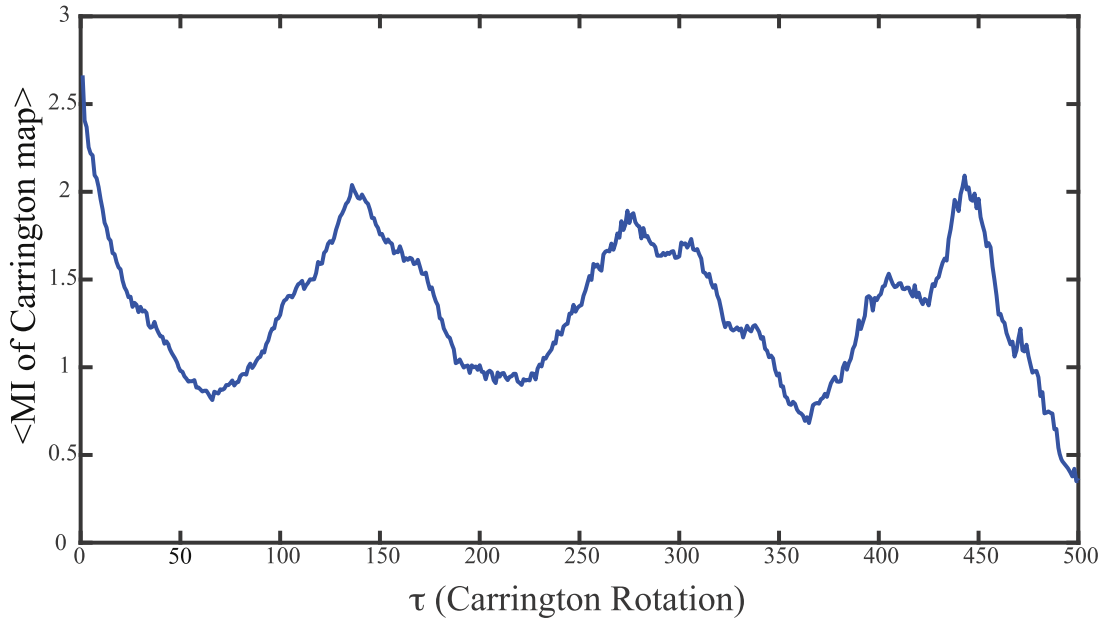


Figure 3. Ensemble average of the mutual information of a sequence of images: $\text{MI}(c(t), c(t + \tau))$ where $c(t)$ is the Carrington image at time t and τ is the lag time. The MI peaks at $\tau \sim 140 \times n$ where $n = \text{integer}$. In other words, MI peaks at every integer multiplication of a solar cycle period.

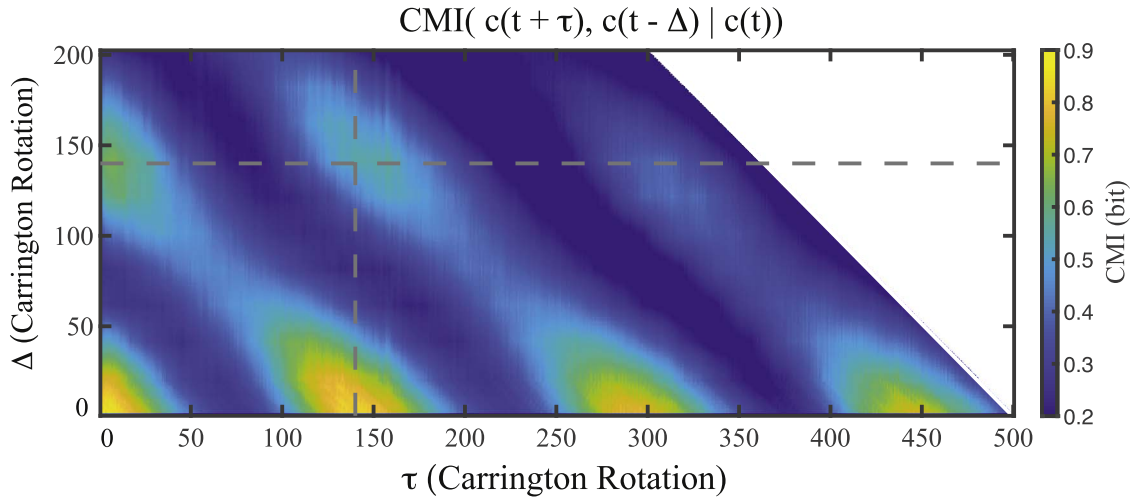


Figure 4. Conditional mutual information between Carrington maps at look ahead τ and look behind Δ . Enhancement in the CMI are at $\tau = \Delta = 140$, where the dashed gray lines intersect, suggests a long-term memory of two solar cycles in duration.

of the structures. To do this, we apply a neighborhood averaging filter that effectively averages over larger and larger regions of the image. The mutual information should peak when the averaging filter corresponds to the size of the structures. The mutual information would be smaller when there is more random variation in the pixels (too much resolution) and when there is not enough variation in the pixels (too little resolution). The results are shown in Figure 5. The figure shows that there is a peak when the scale size of the averaging filter is 32–64 square pixel. Each pixel corresponds to 5° resolution (around 3686 Mm^2) and hence, the strongest mutual information occurs on a scale of 118×10^3 – $236 \times 10^3 \text{ Mm}^2$, which perhaps corresponds approximately to the scale size of the active region structures that carry the most information.

7. Summary and Conclusion

We apply information theory to examine information flow and nonlinear dynamics in the solar active regions. Such an analysis can characterize the periodicities and memories of the underlying dynamical process of the driving dynamo and to determine predictability of the system. The analysis is based on the image entropies of the Carrington maps from 597 Carrington rotations 1974 to 2021 spanning solar cycles 21–24. An innovative aspect of this study is using the entropy filter to identify active region partitions, which are then registered for each image. The mutual information for these partitions are computed, which makes it possible to follow structures that are coherent, yet moving (due to differential rotation), in sequences of maps.

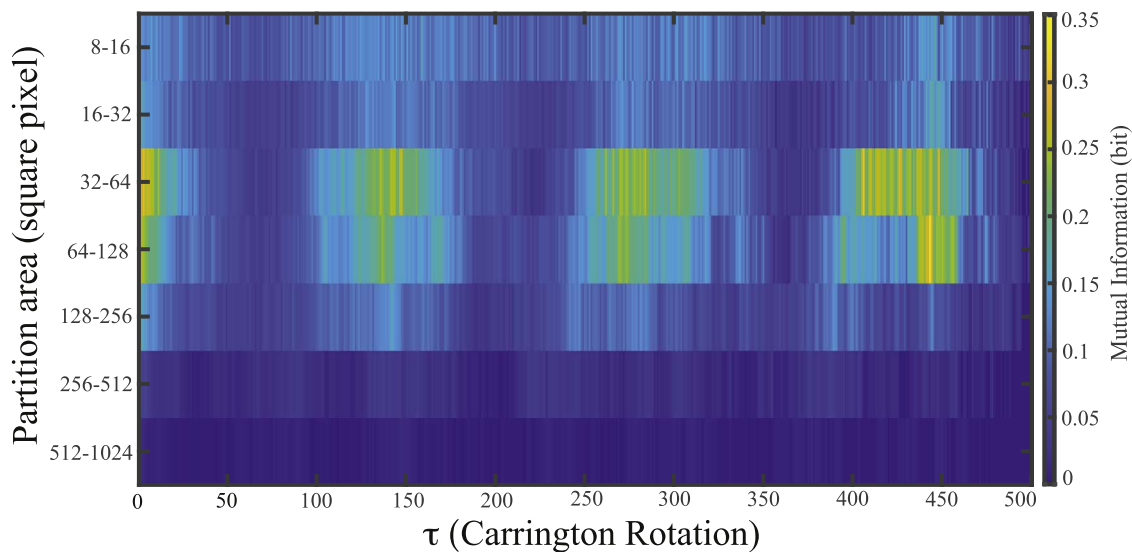


Figure 5. Mutual information as a function of neighborhood averaging filter size and τ . The maximum mutual information is found for filter with 32–64 square pixels (118×10^3 – 236×10^3 Mm²), suggesting approximately the average scale of the active region structures.

Our analysis shows that the Sun has many intrinsic oscillation modes and memories. We list below three key findings.




1. The Sun exhibits a long-term memory of two cycles or more.
2. The coherence (short-term memory) timescale of the active region structures is about ~ 2 yr.
3. The average active region structure scale size carrying the most information is approximately 118×10^3 – 236×10^3 Mm².

The results have implications to the short- and long-term predictability of the active region structures and by extension sunspot structures (Pesnell 2016). In particular, for the long-term prediction, our analysis provides evidence and hope that at least in a statistical sense, it may be possible to predict some aspects of the active region structures more than one or two solar cycles ahead. Our study also has implications to the nature of the convection and flux transport at the Sun.

Our innovative method can also be applied to the light curves of stellar data. Each light curve has oscillations that correspond to stellar rotation (the analog of Carrington rotations) and changes in the light curves result primarily from the starspots, flares, or planetary transits. By comparing light curves for each rotation, we can also investigate the evolution of the stellar active regions and see how that evolution compares with the Sun.

We acknowledge the support of NASA Grants 80NSSC21K1678, 80NSSC20k0355, 80NSSC20K0704, 80NSSC22K0515, and NNX16AQ87G.

ORCID iDs

Jay R. Johnson  <https://orcid.org/0000-0002-9562-1103>
 Simon Wing  <https://orcid.org/0000-0001-9342-1813>
 Bishwa Neupane  <https://orcid.org/0000-0002-1464-3635>

References

Babcock, H. W. 1961, *ApJ*, 133, 572
 Bai, T. 1987, *ApJ*, 314, 795

Balasis, G., Donner, R. V., Potirakis, S. M., et al. 2013, *Entrop*, 15, 4844
 Barnhart, B. L., & Eichinger, W. E. 2011, *SoPh*, 269, 439
 Beer, J., Tobias, S., & Weiss, N. 1998, *SoPh*, 181, 237
 Cameron, R. H., & Schüssler, M. 2016, *A&A*, 591, A46
 Charbonneau, P. 2020, *LRSP*, 17, 4
 Charbonneau, P., & Barlet, G. 2011, *JASTP*, 73, 198
 Charbonneau, P., & Dikpati, M. 2000, *ApJ*, 543, 1027
 Choudhuri, A. R., Chatterjee, P., & Jiang, J. 2007, *PhRvL*, 98, 131103
 De Michelis, P., Tozzi, R., & Consolini, G. 2017, *EP&S*, 69, 24
 Dikpati, M., & Charbonneau, P. 1999, *ApJ*, 518, 508
 Dikpati, M., de Toma, G., Gilman, P. A., Arge, C. N., & White, O. R. 2004, *ApJ*, 601, 1136
 Dikpati, M., & Gilman, P. A. 2006, *ApJ*, 649, 498
 Gnevyshev, M., & Ohl, A. 1948, *AZh*, 25, 18
 Guerrero, G., & de Gouveia Dal Pino, E. M. 2008, *A&A*, 485, 267
 Huang, N. E., & Wu, Z. 2008, *RvGeo*, 46, RG2006
 Jiang, J., Chatterjee, P., & Choudhuri, A. R. 2017, *MNRAS*, 381, 1527
 Johnson, J. R., & Wing, S. 2005, *JGRA*, 110, A04211
 Johnson, J. R., & Wing, S. 2014, *GeoRL*, 41, 5748
 Johnson, J. R., Wing, S., & Camporeale, E. 2018, *AnGeo*, 36, 945
 Knobloch, E., Tobias, S. M., & Weiss, N. O. 1998, *MNRAS*, 297, 1123
 Lean, J. L., & Brueckner, G. E. 1989, *ApJ*, 337, 568
 Leighton, R. B. 1964, *ApJ*, 140, 1547
 Leighton, R. B. 1969, *ApJ*, 156, 1
 McIntosh, S. W., & Leamon, R. J. 2017, *FrASS*, 4, 4
 McIntosh, S. W., Leamon, R. J., Krista, L. D., et al. 2015, *NatCo*, 6, 6491
 Muñoz-Jaramillo, A., Dasi-Espuig, M., Balmaceda, L. A., & DeLuca, E. E. 2013a, *ApJL*, 767, L25
 Muñoz Jaramillo, A., Balmaceda, L. A., & DeLuca, E. E. 2013b, *PhRvL*, 111, 041106
 Osmane, A., Savola, M., Kilpua, E., et al. 2022, *AnGeo*, 40, 37
 Pesnell, W. D. 2016, *SpWea*, 14, 10
 Rivera, E., Johnson, J. R., Homan, J., & Wing, S. 2022a, *A&A*, 670, A143
 Rivera, E. C., Johnson, J. R., Homan, J., & Wing, S. 2022b, *ApJL*, 937, L8
 Snelling, J. M., Johnson, J. R., Willard, J., et al. 2020, *ApJ*, 899, 148
 Tobias, S. M. 1997, *A&A*, 322, 1007
 Wilmot-Smith, A. L., Martens, P. C. H., Nandy, D., Priest, E. R., & Tobias, S. M. 2005, *MNRAS*, 363, 1167
 Wing, S., Brandt, P., Mitchell, D., et al. 2020, *AJ*, 159, 249
 Wing, S., & Johnson, J. R. 2019, *Entrop*, 21, 140
 Wing, S., Johnson, J. R., Camporeale, E., & Reeves, G. D. 2016, *JGRA*, 121, 9378
 Wing, S., Johnson, J. R., Turner, D. L., Ukhorskiy, A. Y., & Boyd, A. J. 2022, *JGRA*, 127, e2021JA030246
 Wing, S., Johnson, J. R., & Vourlidas, A. 2018, *ApJ*, 854, 85
 Yeates, A. R., Nandy, D., & Mackay, D. H. 2008, *ApJ*, 673, 544
 Zaqarashvili, T. V., Carbonell, M., Oliver, R., & Ballester, J. L. 2010, *ApJ*, 709, 749